Electrocatalysis of N-doped Carbons in the Oxygen Reduction Reaction as a function of pH: N-sites and Scaffold Effects

James A. Behan,[a†] Alessandro Iannaci,[a†] Carlota Domínguez,[a] Serban N. Stamatin,[a,b] Md. Khairul Hoque,[a] Joana M. Vasconcelos,[a] Tatiana S. Perova[c] and Paula E. Colavita[a]*

a - School of Chemistry, CRANN and AMBER research centres, Trinity College Dublin, College Green, Dublin 2.

b - Faculty of Physics, 3Nano-SAE Research Centre, University of Bucharest, 405 Atomistilor Str., Bucharest-Magurele 077125, Romania.

c - Department of Electronic and Electrical Engineering, Trinity College Dublin, Dublin 2, Ireland and ITMO University, 49 Kronverskiy pr., Saint Petersburg, 197101, Russia.

[†] Authors contributed equally to this work.

[*] Corresponding author: Tel: 353 1 8963562; Email: colavitp@tcd.ie.

ABSTRACT

Metal-free nitrogenated amorphous carbon electrodes were synthesised via dc plasma magnetron sputtering and post-deposition annealing at different temperatures. The electrocatalytic activity of the electrodes towards the oxygen reduction reaction (ORR) was studied as a function of pH using cyclic voltammetry with a rotating disk electrode. The trends in onset potential were correlated to the carbon nanostructure and chemical composition of the electrodes as determined via Raman spectroscopy and X-ray photoelectron spectroscopy analysis. Results suggest that: 1) the ORR activity in acidic conditions is strongly correlated to the concentration of pyridinic nitrogen sites. 2) At high pH, the presence of graphitic nitrogen sites and a graphitized carbon scaffold are the strongest predictors of high ORR onsets, while pyridinic nitrogen site density does not correlate to ORR activity. An inversion region where pyridine-mediated activity competes with graphitic-N mediated activity is identified in the pH region close to the value of pK_a of the pyridinium cation. The onset of the ORR is therefore determined by the activity of different sites as a function of pH and evidence for distinct reduction reaction pathways emerges from these results.

1. Introduction

The oxygen reduction reaction (ORR) is a cathodic process which is employed in H_2/O_2 fuel cell devices which have been suggested as a green technology to mitigate emissions associated with fossil fuel combustion [1-3]. The implementation of the ORR currently suffers from a number of practical challenges including large overpotentials and the over reliance on precious metal catalysts [2, 4, 5]. Cathodes prepared using the most common catalyst, platinum on carbon (Pt/C), have been estimated to account for up to one half of overall fuel cell costs [6, 7]. Moreover Pt is highly susceptible to poisoning from a number of species including CH_4, CO, MeOH, H_2S, NO_2, and SO_2 [8] and the Pt/C catalyst also suffers from degradation in the form of nanoparticle agglomeration, ripening and detachment from the support [9, 10]. In recent years research has focused on replacing Pt with sustainable alternatives including non-precious metals such as Fe/C, Fe/C-N catalysts [11-14] and metal-free electrocatalysts based on heteroatom doped carbon materials. In the latter category nitrogen-doped carbon materials in particular have shown promise with N-doped carbon nanotubes [2, 15, 16], graphene [17-20], and mesoporous carbon [21] all reported in the literature.

Despite the fact that some N-doped carbons are more active than Pt/C [22-24] under alkaline conditions, the precise reason for this high activity is not well understood. Efforts have been made to identify the active sites for ORR on N-doped carbon using both experimental and theoretical methods [25-28], however these results are far from conclusive. For instance, the presence of pyridinic-N (N_{pyr}) sites has been proposed to correlate to the ORR activity [25, 28, 29]. Graphitic-N (N_G) sites have also been identified as the ones most active in the ORR in both experimental and theoretical studies [7, 30, 31], while several studies have identified both N_G and N_{pyr} as important for the ORR [32, 33]. These studies are however carried out using different types of carbon materials, ranging from graphene to

nanotubes to amorphous carbons, and using aqueous media at differing pH values. A study of pH dependence in the ORR activity using the same carbon electrode materials over the acid to alkaline range to the best of our knowledge has not been undertaken so far using model electrodes. This kind of study might contribute to explaining some of the controversy in this field.

In this work we present a comprehensive study of the ORR activity of N-doped carbon materials as a function of pH. We have used model N-doped carbon electrodes prepared via sputter deposition and thermal treatment; this methodology had been shown by our group to result in excellent model materials with reproducible and smooth topography, low porosity and tunable N-content and N-site type, suitable for mechanistic investigations of carbon electrocatalysis [27],[34]. In this study we have focused on the effect of carbon electrode composition and pH on the onset of the ORR as evaluated using voltammetric studies under acidic and basic conditions as well as at a variety of intermediate values between pH 5 and pH 9. The onset of the ORR at each pH was correlated to the N-site chemistry and carbon scaffold nanostructuring as identified through a combination of XPS and Raman spectroscopy. Our experimental approach provides a simple and clear platform to identify (a) optimal synthetic principles for the design of ORR-active N-doped carbons over a wide pH range, and (b) evidence for a transition in the role of specific N-sites in determining onset behaviour.

2. Experimental Methods

Perchloric Acid (67-72%, Fluka), Sodium Phosphate monobasic and Sodium Phosphate dibasic (≥99.0%, SigmaAldrich) and KOH (semiconductor grade pellets, 99.99%, SigmaAldrich) were all used without further purification.

Glassy carbon disks (Ø 5mm HTW, Germany) were polished with progressively finer grades of alumina slurry (Buehler); further details are reported elsewhere [34]. Thin film electrodes of nitrogenated amorphous carbon (a-C:N) were deposited onto the GC disks via DC plasma magnetron sputtering in a chamber (Torr international) with a base pressure $\leq 2 \times 10^{-6}$ mbar and a deposition pressure in the range $(2-7) \times 10^{-3}$ mbar using a graphite target (99.999%, Lesker, 2.00'' diameter and 0.125'' thickness), as reported previously[27]. Nitrogen was introduced in the carbon scaffold by varying the proportion of N_2/Ar gas during deposition, while keeping a constant total flow. After deposition, the resulting films were transported directly to a tube furnace and annealed under N_2 atmosphere for 1 h at 700 or 900 °C, as illustrated in Figure 1a. A total of four different nitrogenated carbon materials were used in our studies by varying both the N_2/Ar mix (2 or 10%) and the annealing temperature (700 or 900 °C); these four materials are summarised in Table 1, together with the experimental conditions used for their preparation.

Table 1: Nitrogenated carbon electrode materials and experimental conditions used for their deposition and subsequent annealing.

Sample	N (sccm)	Ar (sccm)	$T_{annealing}$ (˚C)
a-C:N-1 a700	1.0	49.0	700
a-C:N-1 a900	1.0	49.0	900
a-C:N-2 a700	5.0	45.0	700
a-C:N-2 a900	5.0	45.0	900

Electrochemical studies were carried out using a three-electrode setup and a potentiostat (Metrohm Autolab AUT50324). The working electrode (a-C:N on GC disks, Table 1) was mounted in a static teflon disc holder (Pine); a Hydroflex hydrogen electrode (Gaskatel) and a graphite rod were used as reference and counter electrodes, respectively, as previously

reported [34]. Measurements were carried out in a jacketed electrochemical cell (Pine Instruments) thermostated at 25 °C. Prior to all experiments, the cell was cleaned using *piranha* solution (*CAUTION: piranha solution can be explosive in contact with organics*), and rinsed with copious amounts of Millipore water [34]. Cyclic voltammograms (CVs) were acquired over 0.05-1.00 V vs RHE in deaerated solutions of $HClO_4$ (pH 1), phosphate buffered solutions (pH 5-9) or KOH (pH 13). A CV in Ar-saturated solution was used to subtract the capacitive background current from the waves obtained in O_2-saturated solutions. Unless otherwise specified, error bars are calculated on the basis of data from four disks for each of the a-C:N materials.

X-ray photoelectron spectroscopy (XPS) was carried out on a VG Scientific ESCAlab MK II system with an Al Kα source at 90° take-off angle. Wide surveys and core level spectra were collected at 50 and 20 eV pass energy, respectively. All spectra were analysed using a commercial software (CasaXPS^{TM}); peaks were fitted with Voigt functions after Shirley background subtraction and atomic %ratios were obtained from peak area ratios after correction by Scofield relative sensitivity factors (C = 1, N = 1.8, O = 2.93). Raman spectra were measured with a Renishaw 1000 micro-Raman system equipped with an Ar^+ laser at 488 nm excitation (backscattering configuration). The incident beam was focused by a Leica microscope with a 50× magnification objective and short-focus working distance; incident power was kept less than 2 mW to avoid sample degradation and spectra were fitted using Origin Lab Origin pro 9.1 software.

3. Results and Discussion

To investigate the effects of N-site type and concentration as well as of carbon scaffold nanostructuring on the ORR activity, we prepared four N-doped carbon model catalysts based on plasma sputtered amorphous carbon films. The synthetic protocol is illustrated in **Figure**

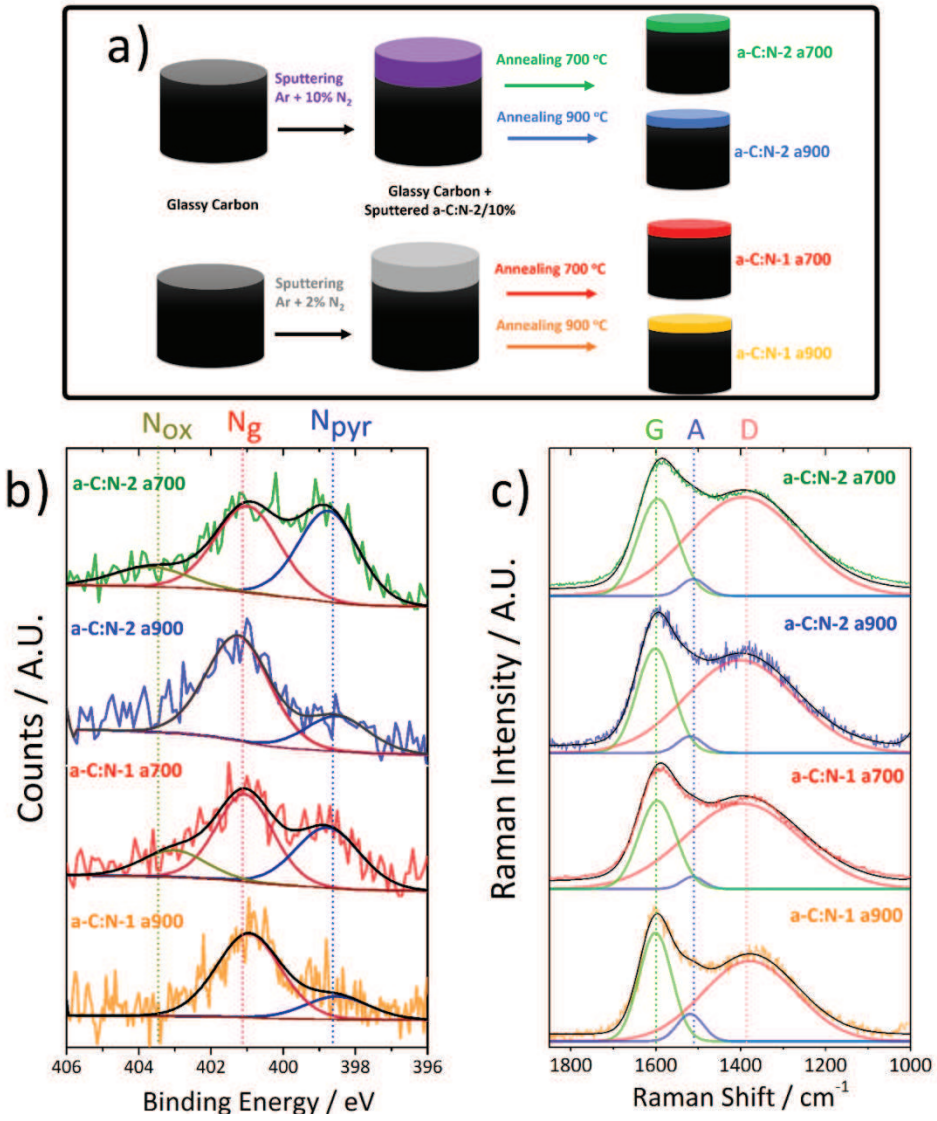

Figure 1. a) Schematic illustrating the preparation of a-C:N-1 a700/a900 and a-C:N-2 a700/a900 electrodes. b) Deconvoluted N 1s spectra of nitrogenated electrodes. Dashed lines indicate the binding energies assigned to N_{pyr}, N_G and N_{ox} peaks. c) Raman spectra of nitrogenated electrodes. The G, D and A peaks are indicated with dashed lines. The raw spectrum and envelope are offset slightly from component peaks for clarity.

1a. Glassy carbon disks were used as the substrate for the deposition of nitrogenated amorphous carbon (a-C:N) thin films according to previously reported protocols [27, 34]. The N-content was varied by altering the N_2/Ar ratio in the plasma deposition gas, resulting in

solid thin films of a-C:N that are uniform and featureless [34] over the geometric area of the disk. Two types of as-deposited a-C:N electrodes were produced using 2% N_2 and 10% N_2; these will henceforth be referred to as a-C:N-1 and a-C:N-2 respectively. After deposition the nanostructure of the a-C:N-1 and -2 electrodes was further modified via thermal annealing in a tube furnace at either 700 ^{o}C or 900 ^{o}C to induce different degrees of graphitization in each carbon scaffold, while preserving the smoothness of the original deposited films (see Supporting Information). The resulting annealed electrodes are referred to as a-C:N-1 a700 / a900 and a-C:N-2 a700 / a900 as shown on the right hand side of **Figure 1a** and as summarised in Table 1.

Table 2. O/C at.%, N/C at.% and %-contribution of graphitic-N (N_G), pyridinic-N (N_{pyr}) and N-O (N_{ox}) sites to the total N 1s peak obtained for model carbon electrodes via XPS.[a]

Sample	O/C %	N/C%	N_G %	N_{pyr} %	N_{ox} %
a-C:N-1 a700	5 ± 3	7.4 ± 0.6	48 ± 8	40 ± 6	11 ± 10
a-C:N-1 a900[b]	4 ± 1	1.8 ± 0.3	75 ± 5	25 ± 5	-
a-C:N-2 a700	6 ± 1	13 ± 2	44 ± 3	44 ±3	12 ± 6
a-C:N-2 a900[b]	2.6 ± 0.7	2.4 ± 0.6	74 ± 8	26 ± 8	-

a – Errors reported are 95% confidence intervals with n = 3 in each case.
b – Results reproduced from Reference [27].

Representative high resolution XPS scans of the N 1s region for each of the four electrodes are shown in **Figure 1b** with the resulting composition data reported in **Table 2.** Survey spectra showing that the electrodes are metal-free and deconvoluted C 1s envelopes are presented in the **Supporting Information.** The N 1s envelopes were fitted using three major contributions: a peak at *ca.* 398.5 eV which may be attributed to pyridinic-N (N_{pyr}) sites, a second peak close to 401 eV which is associated with graphitic-N (N_G), and a third

peak above 402 eV that is evident only in samples annealed at 700 ^{o}C, and that is normally assigned to N-oxide (N_{ox}) moieties [29, 35, 36].

The total N/C at.% is highest in the a700 samples (**Table 2**) with a-C:N-2 a700 possessing the highest N/C at.% of 13 ± 2. Annealing at the higher temperature of 900 ^{o}C results in a total N/C close to 2 at.% in both cases. The N at.% content in our model N-doped carbon electrodes is comparable to that reported for model carbons obtained via ion bombardment of highly oriented pyrolytic graphite (HOPG) and used for the study of the ORR by different research groups [25, 37-40]. The N-site composition obtained after annealing at the two temperatures was found to significantly differ. In a900 samples, the N_G sites are the predominant N-sites **(Table 2**), which is consistent with this moiety being reported as the most stable one at high temperatures [41]. A contribution from N_{pyr} sites of *ca.* 25% is observed in both a900 electrodes whilst no evidence of N_{ox} sites is detected. By contrast, both a700 samples possess roughly equivalent amounts of both N_G and N_{pyr} sites and a minor contribution from N_{ox} sites, since these thermally less-stable moieties are able to survive the annealing process at the lower temperature. Considering the similarities in N-content and composition, the a900 surfaces serve as N-doped carbon model electrode systems with minimal contributions from N_{pyr} and N_{ox} sites to the surface chemistry, whilst the response of the a700 systems can be attributed to contributions from all three types of N-site.

In addition to the differences in surface composition just described, the four N-doped carbon electrodes are also highly distinct from one another in terms of the structural organisation of the carbon scaffold. **Figure 1c** shows deconvoluted Raman spectra of the electrodes in the 1800-1000 cm^{-1} region. Evident in each of the spectra are the typical features of a graphitized amorphous carbon, *viz.* the G peak at *ca.* 1590-1600 cm^{-1} and the D peak at *ca.* 1380 cm^{-1} [42-44]. A small satellite peak at *ca.* 1000 cm^{-1} is observed in some of

the spectra, which may be attributed to the underlying Si substrate on which the Raman samples were deposited [45]. Best fits for each of the spectra were obtained using a 3-peak Gaussian deconvolution; two contributions correspond to the G and D peaks, while a third peak was necessary to fit the shoulder evident in each spectrum at *ca.* 1510 cm^{-1}. This peak is often referred to as the A peak and has been observed in previous work [27, 46]; it is proposed to be due to amorphous regions in the carbon scaffold in between graphitic crystallite domains.

Table 3 summarises the most relevant Raman parameters derived from the deconvolution. All four electrodes display properties consistent with graphitization resulting from the thermal annealing process [42, 43]. In graphitized carbon scaffolds, the D to G peak height ratio, I_D/I_G, is positively correlated to the degree of disorder, as shown by Ferrari et al. [42, 44]. Both of the a700 electrodes display I_D/I_G close to 1, with the a-C:N-2 a700 being the most disordered (I_D/I_G = 1.07). The I_D/I_G values for the a900 samples are significantly lower, with a-C:N-1 a900 having the lowest ratio of all samples (0.73) and the a-C:N-2 a900 material being slightly more disordered (I_D/I_G = 0.84) although still significantly more graphitized than either a700 sample. The lower G peak positions of a700 relative to a900 materials also indicate that the former are less graphitized than a900 samples. A comparison of a-C:N-1 and a-C:N-2 at both annealing temperatures shows that for a given annealing treatment, the more heavily nitrogenated a-C:N-2 samples are more disordered than a-C:N-1. This may be explained in terms of the disorder introduced into the scaffold during the initial nitrogenation process, as this is known to introduce point defects, edges and interruptions in the scaffold associated with the incorporation of N sites [27]. Although much of these sites are removed by the annealing process as discussed above, this does not necessarily result in the complete graphitization of the scaffold. The degree of disorder in the initial structure in each case strongly influences the final structure obtained after the annealing treatment.

Table 3. Raman Parameters of a-C:N-1 a700/a900 and a-C:N-2 a700/a900 Electrodes.

Sample	I_D/I_G	G position / cm^{-1}	D position / cm^{-1}
a-C:N-1 a700	0.95	1591	1397
a-C:N-1 a900[a]	0.73	1600	1379
a-C:N-2 a700	1.07	1596	1400
a-C:N-2 a900[a]	0.84	1603	1385

In summary, we prepared four N-doped carbon model electrodes with different N content and N-site chemistry through the post-deposition annealing of sputtered amorphous carbon films at different temperatures. XPS and Raman data indicated that a lower annealing temperature of 700 ^{o}C results in more disordered carbon materials with higher N content and a greater proportion of pyridinic N-sites. Annealing at the higher temperature of 900 ^{o}C produced more graphitized carbon scaffolds with predominantly graphitic N-sites.

Electrochemical Characterisation

The electrocatalytic activity of all four N-doped carbon materials in the ORR was evaluated in terms of the onset potential (E_{onset}) at varying pH via voltammetry. Figure 2 shows linear sweep voltammograms (LSV) of the four electrodes in 0.1 M $HClO_4$ (**Figure 2a**) and 0.1 M KOH (**Figure 2b**), respectively. An N-free glassy carbon (GC) electrode is also shown in each case for comparison. It is clear from the figure that the activity trends across the four materials is significantly different in the acid and alkaline solutions. The voltammograms in acidic medium show generally poor activity, with the a-C:N-2 a900 having no identifiable ORR onset in the potential window employed and being indistinguishable from the undoped GC electrode. The a-C:N-1 a900 shows some ORR activity, with E_{onset} of 0.12 V_{RHE} at 0.1 mA cm^{-2} and of 0.29 V_{RHE} at 0.001 mA cm^{-2}. By contrast, a-C:N-1 a700 has much better onsets of 0.25 V_{RHE} and of 0.55 V_{RHE} at 0.1 and 0.001

mA cm^{-2}, respectively, which compare very well to values obtained in acid media using other model nitrogenated electrodes [25, 37].

At pH 13 (**Figure 2b**) there is a remarkable inversion of the trend in ORR activity among the four N-doped electrodes. The a-C:N-2 a900 electrode, which had no appreciable ORR activity at pH 1, has the highest ORR onset potential > 0.7 V_{RHE} at pH 13, with similar values obtained for the a-C:N-1 a900 surface. The onset value observed is comparable or better to those typically reported for N-doped nanocarbon electrode materials with high performance under identical pH conditions [2, 47, 48]. By contrast, in this pH, the a700 electrodes have lower

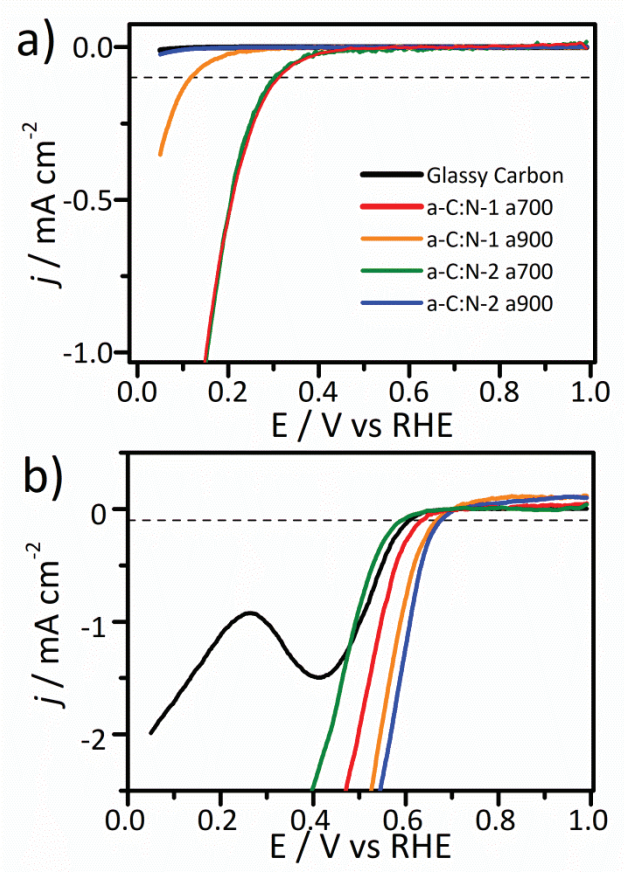

Figure 2. Linear sweep voltammetry (anodic branches) obtained at 2500 rpm of all samples in O_2-saturated 0.1 M $HClO_4$ (a) and 0.1 M KOH (b) solutions after Ar-background subtraction; scan rate 50 mV s^{-1}. The dashed lines in each plot show the current density at 0.1 mA cm^{-2}.

onset potential values < 0.6 V_{RHE}, with the E_{onset} of a-C:N-2 a700 in particular being comparable to the value for N-free GC.

LSV curves were also obtained for the four electrodes in phosphate buffer solutions at intermediate pH values of 5.2, 7.3 and 9.2 as shown in the Supporting Information (**Figure S3**). **Figure 3** shows a summary of the E_{onset} at 0.1 mA cm^{-2} obtained at varying pH, including those at pH 1 and pH 13 discussed above. Notably in this figure, both of the a-C:N a900 electrodes display a nearly linear improvement in E_{onset} with increasing pH. However, for the a-C:N a700 samples, the trend in activity is complex and significantly deviates from a monotonic increase. This is most evident in the case of the a-C:N-1 a700, whose E_{onset}

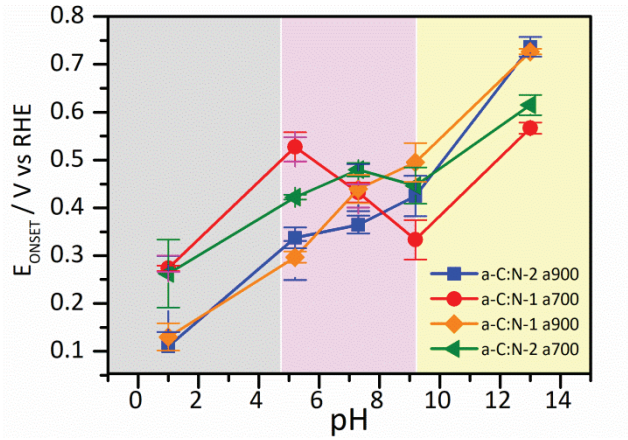

Figure 3. ORR onset potential, E_{onset} for all four N-doped carbon electrodes as function of pH. .

increases over pH 1-5, then decreases between pH 6-8 and subsequently increases up to the highest measured onset at pH 13. A comparison of current densities at potentials 100 mV more cathodic than E_{onset}, i.e. in the mixed mass-transport/kinetic region for all samples, is also shown in the Supporting Information (**Figure S4**). The current density data show that the average *j* values display an overall improvement in alkaline solutions, as is the case of E_{onset}, while being clustered together at all pH values.

The data in **Figure 3** clearly show that a700 materials possess physical/chemical properties that are more advantageous at promoting the onset of ORR than those of a900 materials under acid conditions. This advantage appears to persist up to pH values close to 5-6 while, under basic conditions, the physical/chemical properties of a900 materials confer instead a significant advantage in terms of onset activity. The trend inversion in the intermediate pH region strongly suggests that the type and role of the active sites involved in electrocatalysis of the ORR are pH-dependent.

4. Discussion

Spectroscopic studies of the a-C:N-1 a700/a900 and a-C:N-2 a700/a900 electrodes indicate that these materials differ in their N content, N-site chemistry and carbon scaffold organisation. Many studies of N-doped carbon electrocatalysts have attempted to correlate their ORR performance to specific N sites, with N_{pyr} sites in particular being specified as active sites in acidic media [25, 32, 49-51]. The presence of N_{pyr} sites has been proposed to promote O_2 chemisorption leading to an increased E_{onset} [25, 52]. N-doped carbons have also been shown to display ORR activity under alkaline conditions [53]. In an alkaline environment it has been shown that an alternative mechanism involving reduction of O_2 to superoxide anion ($O_2^{-\bullet}$) in the outer Helmholtz plane is viable; this can be promoted by weak non covalent interactions, which might be present even in the absence of specific chemisorption [30, 54-56].

In the case of charge transfer to an outer sphere species, as is proposed to occur in alkaline environments, changes to the electrode properties that increase carrier density near the Fermi energy should result in improved reduction kinetics. The presence of N_G sites increases the metallic character of carbon electrodes [57], and is thus expected to facilitate outer-sphere reduction processes [34]. The degree of graphitization can also play a role in

modulating charge transfer kinetics: high graphitic content leads to increased metallic character, while the lateral dimension of graphitic clusters is known to affect the density of exposed edges, which display faster kinetics in the ORR than basal planes [58-60]. Finally, the size of graphitic clusters can modulate the Fermi energy position in N-doped carbons thus changing the reductive character of the material, as shown for instance for graphene quantum dots and ball milled graphene electrodes [17, 61].

The more highly graphitised a900 electrodes, which display almost exclusively N_G sites, yield negligible or very poor ORR activity under acidic conditions. However, their E_{onset} improves dramatically as the pH increases until they become the best performers at pH 13. Notably, in the case of a-C:N-1 a900 the E_{onset} varies linearly with a slope of 0.053 V pH^{-1} which is strikingly close to the Nernstian shift vs RHE expected for a pH-independent outer-sphere reduction of O_2 [54]:

$$O_{2\,sol} + e^- \rightarrow O_{2\,sol}^{\bullet -} \qquad (1)$$

which is reported at -0.33 V vs SHE [62]. These findings are consistent with the onset of ORR for N_G-rich materials (a900) being determined by (1), which is predicted to be most sensitive to the electronic properties of the carbon electrode. The role of reaction (1) as the initial step in ORR, has in fact been shown to explain why even N-free carbon electrodes display ORR activity at pH>10 [56].

The a700 electrodes, which contain a much higher proportion of N_{pyr} sites, show the highest onset potentials at pH 1. This result supports the notion that good ORR activity is correlated to the presence of N_{pyr} sites at low pH [25]. However, the dependence of E_{onset} on pH of a700 materials deviates dramatically from a linear trend. This is most pronounced in the case of a-C:N-1 a700 samples: an initial increase in E_{onset} over pH 1-5 is followed by a decrease between pH 6-8 and finally by an increase up to its highest E_{onset} value at pH 13. The overall increase in E_{onset} over pH 1-13 is unsurprising given that these materials were

also found to contain N_G sites which are expected to facilitate the onset of ORR via reaction (1) at high pH. The collapse of E_{onset} in the intermediate pH region (see Figure 3), on the other hand, has not been previously observed in the literature, to the best of our knowledge.

We propose that this behaviour can be attributed to the inactivation of N_{pyr} active sites at pH > 5.2. This value is strikingly close to the pK_a of pyridinium of 5.25 [63]: at pH 1 pyridine moieties are predominantly in the protonated pyridinium form, whereas at pH>6 the lone pair of N_{pyr} sites is mostly deprotonated. The lack of activity at pH 1 displayed by a900 samples further supports the importance of N_{pyr}-sites for the onset of the ORR at low pH. In the intermediate pH region the activity of a700 samples drops significantly while that of a900 ones increases sufficiently so that all four electrodes have similar E_{onset} values at around pH 7. The observed trends are therefore consistent with a progressive deactivation of N_{pyr}-sites that is compensated by an increased importance of N_G-site activity as pH increases and reaction (1) becomes the dominant initial step in the ORR.

Unlike N_G-sites, N_{pyr} sites do not act as proper dopants of the carbon scaffold [57]; this implies that N_G-sites should be preferred over N_{pyr}-sites at high pH, at which the concentration of pyridinium is negligible but the doping effect of N_G remains important. At low pH, at which the outer-sphere electron transfer mechanism is too unfavourable to contribute to the ORR onset [54], the converse is true: protonated N_{pyr} sites are preferable to N_G sites to achieve ORR activity. This is consistent with most studies which point strongly to pyridinic sites as the active domains for N-doped carbon ORR being almost invariably carried out at low pH (see e.g. reference [25]). Computational studies indeed indicate that N_{pyr}-protonation changes the electrophilic character and/or spin density in the adjacent carbon thus facilitating O_2-adsorption [52, 64, 65].

The presence of particular N moieties is not however the only parameter of interest in predicting a high ORR activity. The organisation of the carbon scaffold itself must also

contribute to trends in onset potential. This is most clearly illustrated by a comparison of the E_{onset} for the four electrodes at pH 13 (see **Figures 2 and 3)**: the onset decreases in the order a-C:N-2 a900 = a-C:N-1 a900 > a-C:N-2 a700 > a-C:N-1 a700. The generally higher values of E_{onset} for the a900 samples may appear to contradict the claim that N_G sites promote the ORR at high pH, since both a700 samples possess an overall higher N_G/C%, i.e. a significantly larger density of N_G-sites than both a900 samples.

The superior activity of the a900 samples may be explained by the greater degree of graphitization of the carbon scaffold evident in the Raman data in **Figure 1c** and **Table 3.** The high I_D/I_G values observed for both a700 samples indicate that these materials possess significantly higher disorder and defect density in their scaffolds, which results in a lower metallic character than highly graphitized a900 samples. Thus, even though the a900 samples possess only *ca.* 2% N/C compared to 7.4 % for a-C:N-1 a700 and 14% for a-C:N-2 a700, these N sites are distributed in an overall more graphitic carbon network. This in turn results in a more metallic electrode material which is expected to display facile outer-sphere electron transfer to O_2 [17].

Comparing the response of the two a900 samples at pH 13 to one another, the onset potential is similar, as expected for two materials annealed at the same temperature with comparable N-content and N-site distribution. However the a-C:N-2 a700 has a higher E_{onset} at pH 13 than a-C:N-1 a700, even though both a700 samples were subjected to the same annealing treatment. In this case the higher N/C content (and therefore higher density of N_G sites) of the a-C:N-2 a700 is likely the determining factor. Thus, both N content and scaffold organisation are important parameters for promoting ORR activity, with the former being more important for low or poorly graphitized materials and the latter being most relevant in highly graphitized samples subjected to higher temperature annealing treatments.

5. Conclusions

The electrocatalytic behaviour of model nitrogenated carbon thin film electrodes with controlled N/C content and N_{pyr}/N_g composition was evaluated in the ORR by cyclic voltammetry as a function of pH. Using post deposition annealing it was also possible to vary the degree of graphitisation in the carbon material. Results show that higher annealing temperatures select for materials with predominantly N_g-sites and high graphitic content. Lower annealing temperatures yielded instead a mixture of N_{pyr} and N_g sites and greater disorder/defects in the graphitic structure.

The most graphitic and N_g-rich electrodes display a nearly linear improvement in E_{onset} vs pH; this trend is consistent with the onset potential of the ORR being determined by an outer-sphere electron transfer to yield the superoxide anion [54]. At low pH the activity of the same materials is poor or non-existent, thus confirming that N_g-sites cannot catalyse the ORR in acidic environment.

On the other hand, the materials that display a high concentration of N_{pyr}-sites and high defect concentrations show a dramatically different trend, with good onset potentials at low pH and a collapse of activity at near-neutral and alkaline pH values. Experiments at intermediate pH values identify an inversion region in the ORR activity for those materials possessing a high N_{pyr} density. We propose this to arise because of a deactivation of the protonated form of pyridinic sites (pyridinium cation); this hypothesis is supported by the collapse of the onset potential occurring at a pH that matches the pK_a of pyridinium. In the inversion region near neutral pH, a convergence of onset potentials for all four materials is observed. In this region, the progressive inactivation of pyridinic sites occurs in parallel with a progressive enhancement of the role of graphitic sites, which in their role as dopants can enhance the onset potential via reaction (1).

The complex trends in onset potential observed in our work as a function of pH and N_g/N_{pyr} composition might partly explain the origin of some of the contradicting results reported in the literature on the role of specific N-moieties. The two N-sites play important roles and can become the dominant site depending on the pH region investigated. A further interplay with the graphitic nanostructuring in the carbon scaffold is also important in determining the observed onsets, particularly at high pH. Our results therefore clarify what might be optimal compositional principles for synthetic nitrogenated carbon electrodes for the ORR at different operating pH values.

Acknowledgements

This publication has emanated from research conducted with the financial support of Science Foundation Ireland under Grant No. 13/CDA/2213. JAB acknowledges support from the Irish Research Council under Grant No. GOIPG/2014/399. This project has received funding from the European Union's Horizon 2020 research and innovation programme under the Marie Skłodowska-Curie grant agreements No. 748968 (FREMAB) and 799175 (HiBriCarbon). The results of this publication reflect only the authors' view and the Commission is not responsible for any use that may be made of the information it contains.

REFERENCES

[1] Zhang J. PEM Fuel Cell Electrocatalysts and Catalyst Layers Fundamentals and Applications: Springer; 2008.

[2] Chen Z, Higgins D, Chen Z. Nitrogen doped carbon nanotubes and their impact on the oxygen reduction reaction in fuel cells. Carbon. 2010;48(11):3057-65.

[3] Bezerra CWB, Zhang L, Lee K, Liu H, Marques ALB, Marques EP, et al. A review of Fe–N/C and Co–N/C catalysts for the oxygen reduction reaction. Electrochim Acta. 2008;53(15):4937-51.

[4] Nørskov JK, Rossmeisl J, Logadottir A, Lindqvist L, Kitchin JR, Bligaard T, et al. Origin of the Overpotential for Oxygen Reduction at a Fuel-Cell Cathode. J Phys Chem B. 2004;108(46):17886-92.

[5] Debe MK. Electrocatalyst approaches and challenges for automotive fuel cells. Nature. 2012;486(7401):43.

[6] K. Ben Liew WRWD, M. Ghasemi, J.X. Leong, S.S. Lim, M. Ismail. Non-Pt catalyst as oxygen reduction reaction in microbial fuel cells: A review. Int J Hydrogen Energy. 2014;39.

[7] Sgroi M, Zedde F, Barbera O, Stassi A, Sebastián D, Lufrano F, et al. Cost Analysis of Direct Methanol Fuel Cell Stacks for Mass Production. Energies. 2016;9(12):1008.

[8] Zhang S, Yuan X-Z, Hin JNC, Wang H, Friedrich KA, Schulze M. A review of platinum-based catalyst layer degradation in proton exchange membrane fuel cells. J Power Sources. 2009;194(2):588-600.

[9] Hansen TW, DeLaRiva AT, Challa SR, Datye AK. Sintering of Catalytic Nanoparticles: Particle Migration or Ostwald Ripening? Acc Chem Res. 2013;46(8):1720-30.

[10] Prestat E, Popescu R, Blank H, Schneider R, Gerthsen D. Coarsening of Pt nanoparticles on amorphous carbon film. Surf Sci. 2013;609:195-202.

[11] Bo XJ, Li M, Han C, Zhang YF, Nsabimana A, Guo LP. Noble metal-free electrocatalysts for the oxygen reduction reaction based on iron and nitrogen-doped porous graphene. J Mater Chem A. 2015;3(3):1058-67.

[12] Choi JY, Higgins D, Jiang GP, Hsu R, Qiao JL, Chen ZW. Iron-tetracyanobenzene complex derived non-precious catalyst for oxygen reduction reaction. Electrochim Acta. 2015;162:224-9.

[13] Dong QQ, Zhuang XD, Li Z, Li B, Fang B, Yang CZ, et al. Efficient approach to iron/nitrogen co-doped graphene materials as efficient electrochemical catalysts for the oxygen reduction reaction. J Mater Chem A. 2015;3(15):7767-72.

[14] Yang ZR, Wu J, Zheng XJ, Wang ZJ, Yang RZ. Enhanced catalytic activity for the oxygen reduction reaction with co-doping of phosphorus and iron in carbon. J Power Sources. 2015;277:161-8.

[15] Chen Z, Higgins D, Tao H, Hsu RS, Chen Z. Highly active nitrogen-doped carbon nanotubes for oxygen reduction reaction in fuel cell applications. J Phys Chem C. 2009;113(49):21008-13.

[16] Feng L, Yan Y, Chen Y, Wang L. Nitrogen-doped carbon nanotubes as efficient and durable metal-free cathodic catalysts for oxygen reduction in microbial fuel cells. Energy Environ Sci. 2011;4(5):1892-9.

[17] Choi CH, Lim H-K, Chung MW, Park JC, Shin H, Kim H, et al. Long-Range Electron Transfer over Graphene-Based Catalyst for High-Performing Oxygen Reduction Reactions: Importance of Size, N-doping, and Metallic Impurities. J Am Chem Soc. 2014;136(25):9070-7.

[18] Liang J, Jiao Y, Jaroniec M, Qiao SZ. Sulfur and nitrogen dual-doped mesoporous graphene electrocatalyst for oxygen reduction with synergistically enhanced performance. Angew Chem, Int Ed. 2012;51(46):11496-500.

[19] Qu L, Liu Y, Baek J-B, Dai L. Nitrogen-doped graphene as efficient metal-free electrocatalyst for oxygen reduction in fuel cells. ACS Nano. 2010;4(3):1321-6.

[20] Shao Y, Zhang S, Engelhard MH, Li G, Shao G, Wang Y, et al. Nitrogen-doped graphene and its electrochemical applications. J Mater Chem. 2010;20(35):7491-6.

[21] Liu R, Wu D, Feng X, Müllen K. Nitrogen-Doped Ordered Mesoporous Graphitic Arrays with High Electrocatalytic Activity for Oxygen Reduction. Angew Chem. 2010;122(14):2619-23.

[22] Gong K, Du F, Xia Z, Durstock M, Dai L. Nitrogen-Doped Carbon Nanotube Arrays with High Electrocatalytic Activity for Oxygen Reduction. Science. 2009;323(5915):760-4.

[23] Li Y, Zhou W, Wang H, Xie L, Liang Y, Wei F, et al. An oxygen reduction electrocatalyst based on carbon nanotube–graphene complexes. Nat Nanotechnol. 2012;7(6):394.

[24] Wei W, Liang H, Parvez K, Zhuang X, Feng X, Müllen K. Nitrogen-Doped Carbon Nanosheets with Size-Defined Mesopores as Highly Efficient Metal-Free Catalyst for the Oxygen Reduction Reaction. Angew Chem. 2014;126(6):1596-600.

[25] Guo D, Shibuya R, Akiba C, Saji S, Kondo T, Nakamura J. Active sites of nitrogen-doped carbon materials for oxygen reduction reaction clarified using model catalysts. Science. 2016;351(6271):361-5.

[26] Maldonado S, Stevenson KJ. Influence of nitrogen doping on oxygen reduction electrocatalysis at carbon nanofiber electrodes. J Phys Chem B. 2005;109(10):4707-16.

[27] Behan JA, Hoque MK, Stamatin SN, Perova TS, Vilella-Arribas L, García-Melchor M, et al. Experimental and Computational Study of Dopamine as an Electrochemical Probe of the Surface Nanostructure of Graphitized N-Doped Carbon. J Phys Chem C. 2018;122(36):20763-73.

[28] Wiggins-Camacho JD, Stevenson KJ. Mechanistic discussion of the oxygen reduction reaction at nitrogen-doped carbon nanotubes. J Phys Chem C. 2011;115(40):20002-10.

[29] Chen J, Wang X, Cui X, Yang G, Zheng W. Amorphous carbon enriched with pyridinic nitrogen as an efficient metal-free electrocatalyst for oxygen reduction reaction. Chem Commun. 2014;50(5):557-9.

[30] Yu L, Pan X, Cao X, Hu P, Bao X. Oxygen reduction reaction mechanism on nitrogen-doped graphene: A density functional theory study. J Catal. 2011;282(1):183-90.

[31] Ikeda T, Hou Z, Chai G-L, Terakura K. Possible Oxygen Reduction Reactions for Graphene Edges from First Principles. J Phys Chem C. 2014;118(31):17616-25.

[32] Wu K-H, Wang D-W, Zong X, Zhang B, Liu Y, Gentle IR, et al. Functions in cooperation for enhanced oxygen reduction reaction: the independent roles of oxygen and nitrogen sites in metal-free nanocarbon and their functional synergy. J Mater Chem A. 2017;5(7):3239-48.

[33] Kim H, Lee K, Woo SI, Jung Y. On the mechanism of enhanced oxygen reduction reaction in nitrogen-doped graphene nanoribbons. Phys Chem Chem Phys. 2011;13(39):17505-10.

[34] Behan JA, Stamatin SN, Hoque MK, Ciapetti G, Zen F, Esteban-Tejeda L, et al. Combined Optoelectronic and Electrochemical Study of Nitrogenated Carbon Electrodes. J Phys Chem C. 2017;121(12):6596-604.

[35] Titantah JT, Lamoen D. Carbon and nitrogen 1s energy levels in amorphous carbon nitride systems: XPS interpretation using first-principles. Diamond Relat Mater. 2007;16(3):581-8.

[36] Hellgren N, Haasch RT, Schmidt S, Hultman L, Petrov I. Interpretation of X-ray photoelectron spectra of carbon-nitride thin films: New insights from in situ XPS. Carbon. 2016;108:242-52.

[37] Favaro M, Perini L, Agnoli S, Durante C, Granozzi G, Gennaro A. Electrochemical behavior of N and Ar implanted highly oriented pyrolytic graphite substrates and activity toward oxygen reduction reaction. Electrochim Acta. 2013;88:477-87.

[38] Kiuchi H, Kondo T, Sakurai M, Guo D, Nakamura J, Niwa H, et al. Characterization of nitrogen species incorporated into graphite using low energy nitrogen ion sputtering. Phys Chem Chem Phys. 2016;18(1):458-65.

[39] Pylypenko S, Queen A, Olson TS, Dameron A, O'Neill K, Neyerlin KC, et al. Tuning Carbon-Based Fuel Cell Catalyst Support Structures via Nitrogen Functionalization. II. Investigation of Durability of Pt–Ru Nanoparticles Supported on Highly Oriented Pyrolytic Graphite Model Catalyst Supports As a Function of Nitrogen Implantation Dose. J Phys Chem C. 2011;115(28):13676-84.

[40] Pylypenko S, Queen A, Olson TS, Dameron A, O'Neill K, Neyerlin KC, et al. Tuning Carbon-Based Fuel Cell Catalyst Support Structures via Nitrogen Functionalization. I. Investigation of Structural and Compositional Modification of Highly Oriented Pyrolytic Graphite Model Catalyst Supports as a Function of Nitrogen Implantation Dose. J Phys Chem C. 2011;115(28):13667-75.

[41] Ajay K, Abhijit G, Pagona P. Thermal stability study of nitrogen functionalities in a graphene network. J Phys: Condens Matter. 2012;24(23):235503.

[42] Ferrari AC, Rodil SE, Robertson J. Interpretation of infrared and Raman spectra of amorphous carbon nitrides. Phys Rev B. 2003;67(15):155306.

[43] Ferrari AC, Robertson J. Raman spectroscopy of amorphous, nanostructured, diamond-like carbon, and nanodiamond. Philos T R Soc A. 2004;362(1824):2477-512.

[44] Ferrari AC, Robertson J. Interpretation of Raman spectra of disordered and amorphous carbon. Phys Rev B. 2000;61(20):14095-107.

[45] Ferrari AC, Robertson J. Resonant Raman spectroscopy of disordered, amorphous, and diamondlike carbon. Phys Rev B. 2001;64(7):075414.

[46] Laidani N, Guzman L, Miotello A, Brusa RS, Karwasz GP, Zecca A, et al. Nitrogen effects on the microstructural evolution of carbon films under thermal annealing. Nucl Instrum Methods Phys Res, Sect B. 1997;122(3):553-8.

[47] Bera B, Chakraborty A, Kar T, Leuaa P, Neergat M. Density of States, Carrier Concentration, and Flat Band Potential Derived from Electrochemical Impedance Measurements of N-Doped Carbon and Their Influence on Electrocatalysis of Oxygen Reduction Reaction. J Phys Chem C. 2017;121(38):20850-6.

[48] Ratso S, Kruusenberg I, Käärik M, Kook M, Saar R, Pärs M, et al. Highly efficient nitrogen-doped carbide-derived carbon materials for oxygen reduction reaction in alkaline media. Carbon. 2017;113:159-69.

[49] Li Y, Zhong G, Yu H, Wang H, Peng F. O 2 and H 2 O 2 transformation steps for the oxygen reduction reaction catalyzed by graphitic nitrogen-doped carbon nanotubes in acidic electrolyte from first principles calculations. Phys Chem Chem Phys. 2015;17(34):21950-9.

[50] McClure JP, Thornton JD, Jiang R, Chu D, Cuomo JJ, Fedkiw PS. Oxygen Reduction on Metal-Free Nitrogen-Doped Carbon Nanowall Electrodes. J Electrochem Soc. 2012;159(11):F733-F42.

[51] Xing T, Zheng Y, Li LH, Cowie BCC, Gunzelmann D, Qiao SZ, et al. Observation of Active Sites for Oxygen Reduction Reaction on Nitrogen-Doped Multilayer Graphene. ACS Nano. 2014;8(7):6856-62.

[52] Zhang L, Xia Z. Mechanisms of Oxygen Reduction Reaction on Nitrogen-Doped Graphene for Fuel Cells. J Phys Chem C. 2011;115(22):11170-6.

[53] Wan K, Yu Z-p, Li X-h, Liu M-y, Yang G, Piao J-h, et al. pH Effect on Electrochemistry of Nitrogen-Doped Carbon Catalyst for Oxygen Reduction Reaction. ACS Catal. 2015;5(7):4325-32.

[54] Blizanac BB, Ross PN, Markovic NM. Oxygen electroreduction on Ag(111): The pH effect. Electrochim Acta. 2007;52(6):2264-71.

[55] Ramaswamy N, Mukerjee S. Influence of Inner- and Outer-Sphere Electron Transfer Mechanisms during Electrocatalysis of Oxygen Reduction in Alkaline Media. J Phys Chem C. 2011;115(36):18015-26.

[56] Yang HH, McCreery RL. Elucidation of the Mechanism of Dioxygen Reduction on Metal-Free Carbon Electrodes. J Electrochem Soc. 2000;147(9):3420-8.

[57] Robertson J, Davis CA. Nitrogen Doping of Tetrahedral Amorphous-Carbon. Diamond Relat Mater. 1995;4(4):441-4.

[58] Stamatin SN, Hussainova I, Ivanov R, Colavita PE. Quantifying Graphitic Edge Exposure in Graphene-Based Materials and Its Role in Oxygen Reduction Reactions. ACS Catal. 2016;6(8):5215-21.

[59] Yan D, Li Y, Huo J, Chen R, Dai L, Wang S. Defect Chemistry of Nonprecious-Metal Electrocatalysts for Oxygen Reactions. Adv Mater (Weinheim, Ger). 2017;29(48):1606459.

[60] Shen A, Zou Y, Wang Q, Dryfe RAW, Huang X, Dou S, et al. Oxygen Reduction Reaction in a Droplet on Graphite: Direct Evidence that the Edge Is More Active than the Basal Plane. Angew Chem, Int Ed. 2014;53(40):10804-8.

[61] Li Q, Zhang S, Dai L, Li L-s. Nitrogen-Doped Colloidal Graphene Quantum Dots and Their Size-Dependent Electrocatalytic Activity for the Oxygen Reduction Reaction. J Am Chem Soc. 2012;134(46):18932-5.

[62] Bard AJ, Parsons R, Jordan J. Standard Potentials in Aqueous Solution: Marcel Dekker, Inc.; 1985.

[63] Kerr J, Lide D. CRC handbook of chemistry and physics 1999–2000: a ready-reference book of chemical and physical data. CRC Handbook of Chemistry and Physics. 2000.

[64] Hisayoshi K, Nakzono T, Soichi M, Toshiko M, Nobuyuki T, Tokio Y. DFT Study of Oxygen Reduction Reaction on N-substituted Carbon Electrodes. Adsorption. IOP Conference Series: Materials Science and Engineering. 2011;18(12):122010.

[65] Feng X. Nanocarbons for Advanced Energy Conversion: John Wiley & Sons; 2015.

Figure 1
Click here to download high resolution image

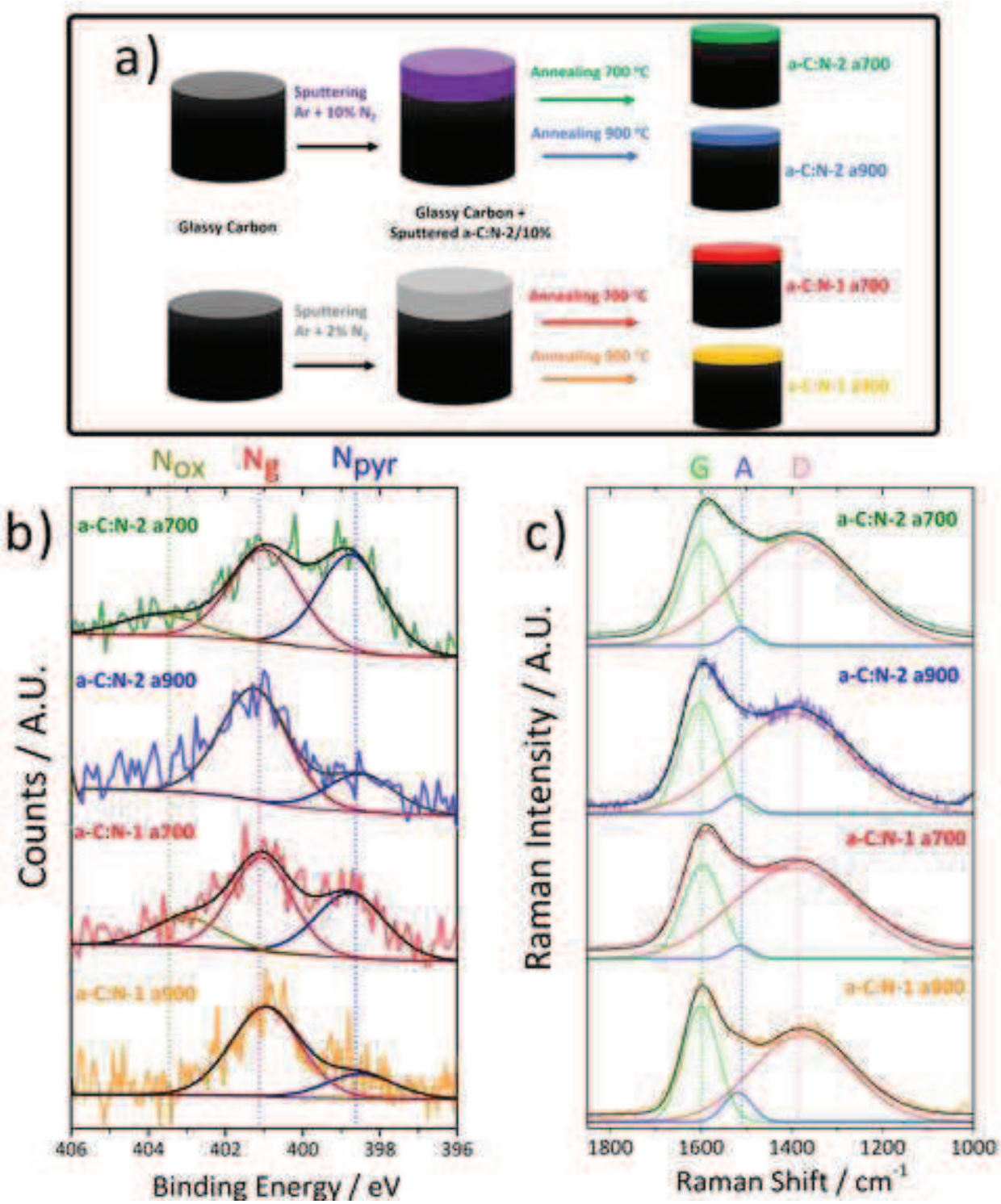

Figure 2
Click here to download high resolution image

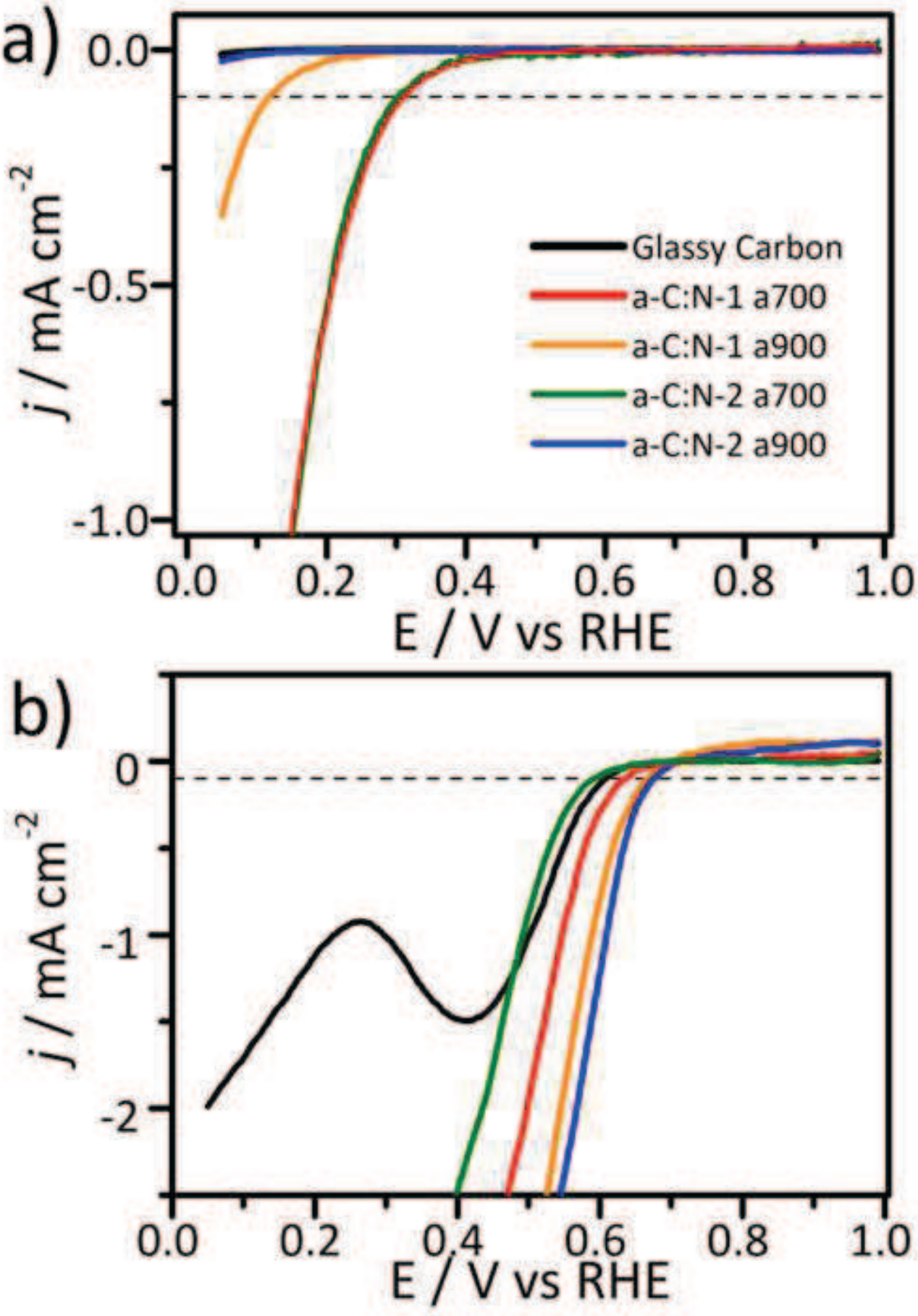

Figure 3
Click here to download high resolution image

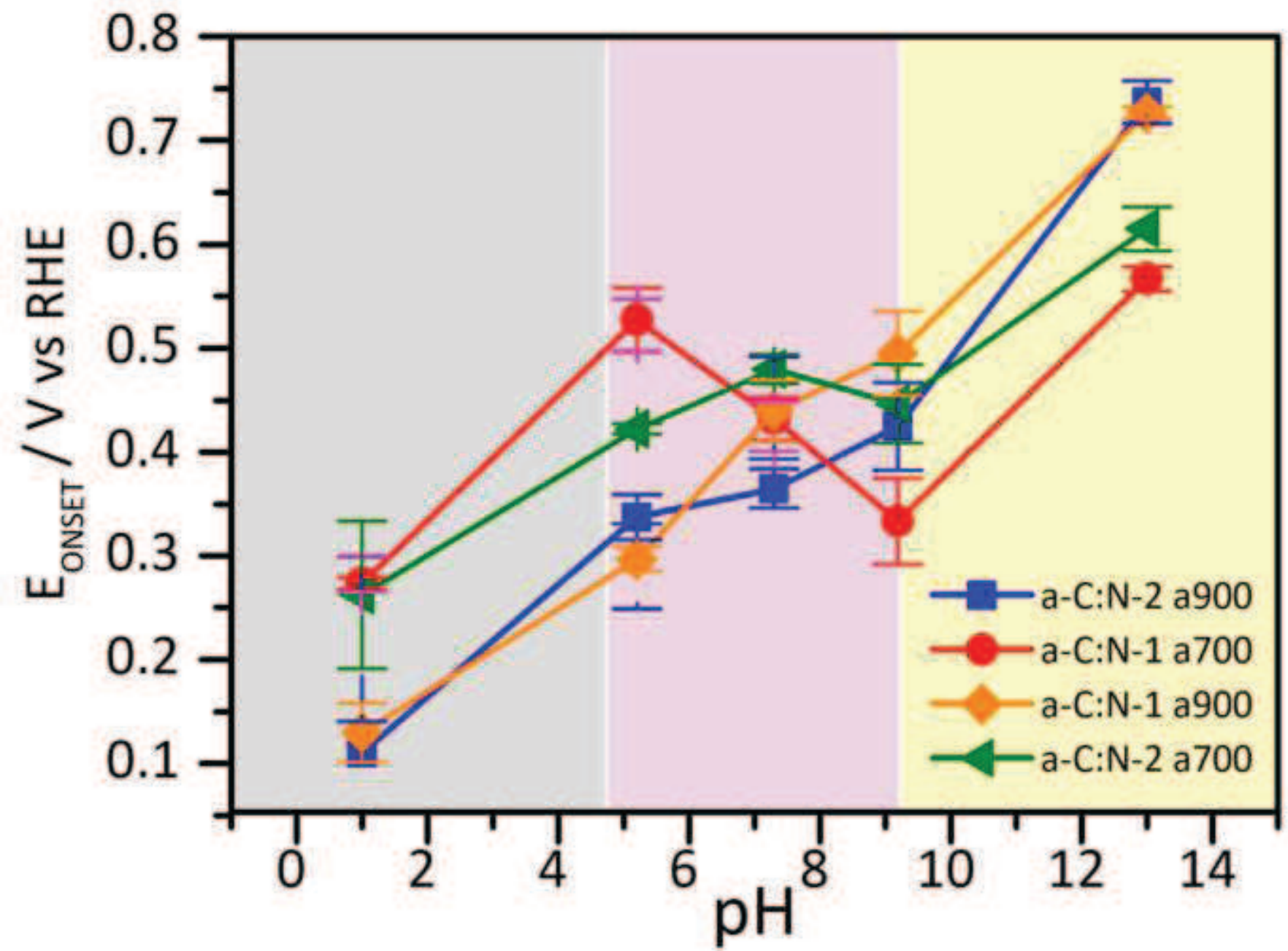

*Graphical Abstract

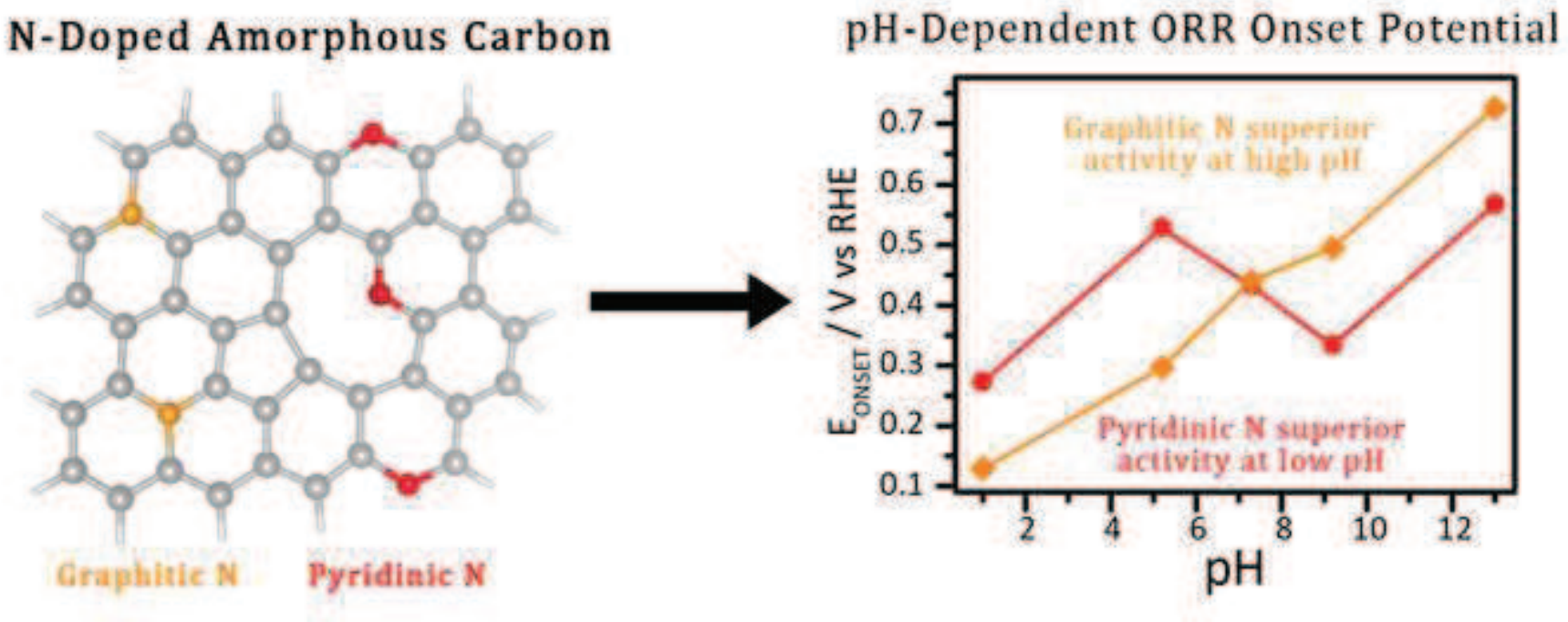

Supplementary Material

Click here to download Supplementary Material: 20190225_Supporting Information_Revised.docx